

ORIGINAL ARTICLE

Multi-photon quantum cutting in $\text{Gd}_2\text{O}_2\text{S:Tm}^{3+}$ to enhance the photo-response of solar cells

De-Chao Yu^{1,2}, Rosa Martín-Rodríguez², Qin-Yuan Zhang¹, Andries Meijerink², and Freddy T Rabouw²

Conventional photoluminescence (PL) yields at most one emitted photon for each absorption event. Downconversion (or quantum cutting) materials can yield more than one photon by virtue of energy transfer processes between luminescent centers. In this work, we introduce $\text{Gd}_2\text{O}_2\text{S:Tm}^{3+}$ as a multi-photon quantum cutter. It can convert near-infrared, visible, or ultraviolet photons into two, three, or four infrared photons of ~ 1800 nm, respectively. The cross-relaxation steps between Tm^{3+} ions that lead to quantum cutting are identified from (time-resolved) PL as a function of the Tm^{3+} concentration in the crystal. A model is presented that reproduces the way in which the Tm^{3+} concentration affects both the relative intensities of the various emission lines and the excited state dynamics and providing insight in the quantum cutting efficiency. Finally, we discuss the potential application of $\text{Gd}_2\text{O}_2\text{S:Tm}^{3+}$ for spectral conversion to improve the efficiency of next-generation photovoltaics.

Light: Science & Applications (2015) 4, e344; doi:10.1038/lisa.2015.117; published online 23 October 2015

Keywords: downconversion; infrared emission; quantum cutting; solar cells; spectral conversions

INTRODUCTION

Over the last decade, advanced luminescent materials exhibiting downconversion, also known as quantum cutting or quantum splitting, have been developed^{1,2}. In this process, a high-energy photon is converted into two or more lower-energy photons, with a quantum efficiency of potentially well over 100%³. If the downconverted photons are in the visible range, this concept is of interest for color conversion layers in conventional lighting applications^{1,2,4–6}. New exciting possibilities of downconversion to infrared (IR) photons lie in next-generation photovoltaics, aiming at minimizing the spectral mismatch losses in solar cells^{7–11}.

Spectral mismatch is the result of the broad width of the spectrum emitted by the sun. Semiconductor absorber materials absorb only photons with an energy $h\nu$ higher than the band gap E_g ⁷. To absorb many photons and produce a large electrical current, absorber materials must therefore have a small bandgap. However, because excited charge carriers rapidly thermalize to the edges of a semiconductor's conduction and valence bands, a high voltage output requires an absorber with a large band gap. Hence, materials with low transmission losses (leading to a large current) have high thermalization losses (leading to a low voltage) and vice versa^{12,13}. These spectral mismatch losses constitute the major factor defining the relatively low Shockley–Queisser limit¹⁴, the maximum light-to-electricity conversion efficiency of 33% in a single-junction solar cell, obtained for a band gap of approximately 1.1 eV (1100 nm)¹³.

Efficiencies higher than 33% can be reached with multi-junction solar cells, where a stack of multiple absorber materials are each optimized to efficiently convert different parts of the solar spectrum to

electricity^{15,16}. Although efficiencies of greater than 40% have been obtained with this concept¹⁶, the devices are expensive and have limited tunability because of the requirement of high-quality contacts between absorber materials with matching physical and chemical properties.

An alternative solution to beat the Shockley–Queisser limit is by optical conversion of the solar spectrum prior to entering the solar cell^{2,7–11}. A large number of downconversion materials able to convert high-energy photons into multiple lower-energy photons have recently been developed^{17–32}. The downconversion process occurs by energy transfer between luminescent centers, either lanthanide ions with a wide range of energy levels or organic molecules with low-energy triplet states^{31,32}. If the IR photons generated are all absorbed by the solar cell material, the result can be a huge increase in the current output^{10–13,33}. This concept does not impose requirements on the contact surface between the conversion layer and the solar cell, so it can relatively easily be integrated into existing solar cell technologies.

In this work, we introduce the quadruple-downconversion material $\text{Gd}_2\text{O}_2\text{S:Tm}^{3+}$. Depending on the excitation energy, it can yield two, three, or even four IR photons (mainly approximately 1800 nm) per absorption event. The high-energy photons are cut by a series of cross-relaxation steps, where the initially excited Tm^{3+} ion transfers part of its energy to a neighboring Tm^{3+} . By examining the emission spectra and dynamics as a function of Tm^{3+} concentration in the $\text{Gd}_2\text{O}_2\text{S}$ host crystal, we determine the operative cross-relaxation processes leading to four-photon quantum cutting and quantify the rates and efficiencies. We find that at a moderate Tm^{3+} concentration of 10%, the excitation energy is very efficiently cut into IR quanta (in the $^3\text{H}_5$ level emitting at 1215 nm and in the $^3\text{F}_4$ level emitting at 1800 nm), with efficiencies of

¹State Key Laboratory of Luminescence Materials and Devices and Institute of Optical Communication Materials, South China University of Technology, Guangzhou 510641, China and ²Debye Institute for Nanomaterials Science, Utrecht University, P.O. Box 80000, 3508 TA Utrecht, the Netherlands

Correspondence: QY Zhang, Email: qyzhang@scut.edu.cn; A Meijerink, Email: a.meijerink@uu.nl

Received 5 March 2015; revised 4 June 2015; accepted 18 June 2015; accepted article preview online 20 June 2015

199% for near-IR excitation at 800 nm, 298% for blue excitation at 470 nm, and 388% for ultraviolet (UV) excitation at 365 nm. We discuss the practical application of this multiple-downconversion material to increase the spectral response of solar cells (in particular Ge, of which the band gap is matched to emission from the $^3\text{F}_4$ level). Efforts should be aimed at reducing losses due to concentration quenching of the $^3\text{F}_4$ level and increasing the absorption by means of a sensitizer. In addition to applications in next-generation photovoltaics, because the excitation can be in the first ‘tissue-transparent spectral window’ of approximately 800 nm and the emission of 1800 nm lies in a spectral window with low tissue absorption and reduced light scattering^{34,35}, the concept of efficient downconversion in Tm^{3+} may be useful for bio-imaging applications.

MATERIALS AND METHODS

$\text{Gd}_2\text{O}_2\text{S}:\text{Tm}^{3+}$ powder samples

Microcrystalline samples of $\text{Gd}_2\text{O}_2\text{S}:\text{Tm}^{3+}$ ($x\%$) with $x = 0.1, 1.0, 5.0$, and 10.0 were prepared for this research by Tailorlux GmbH (Münster, Germany). The crystal structure was confirmed using X-ray powder diffractometry (see Supplementary Fig. S1). $\text{Gd}_2\text{O}_2\text{S}$ has a $P\bar{3}m1$ space group, where Tm^{3+} dopant ions substitute for Gd^{3+} at a site with point symmetry C_{3v} surrounded by four oxygen and three sulfur atoms^{36,37}.

Experimental details

Emission spectra and photoluminescence (PL) decay curves were recorded using an Edinburgh Instruments FLS920 spectrofluorometer equipped with a 450 W xenon lamp. Visible emission was detected by a Hamamatsu R928 photomultiplier tube (400–850 nm). Emission spectra in the IR were recorded on a liquid-nitrogen cooled Hamamatsu R5509-72 photomultiplier tube (1100–1600 nm) and a thermoelectrically cooled G5852 InGaAs PIN photodiode (1500–2100 nm). For PL emission measurements, the samples were excited with the xenon lamp. For PL decay measurements, an optical parametric oscillator (OPO) system (Opotek HE 355 II) pumped by the third harmonic of a Nd:YAG laser (pulse width 10 ns; repetition rate 20 Hz) was used for excitation in the $^3\text{F}_{2,3}$ (Figure 1c) or $^1\text{G}_4$ (Figure 2c) levels. PL decay of the $^1\text{D}_2$ level (Figure 3c) was excited with an Ekspla NR342B-10-SH/DUV OPO system (pulse width 5 ns; repetition rate 10 Hz). All experiments were performed at room temperature.

Modeling the photon yield from downconversion

To model the efficiencies of the downconversion processes in $\text{Gd}_2\text{O}_2\text{S}:\text{Tm}^{3+}$, we use the overview of possible relaxation pathways (see Figures 1b, 2b, and 3b). For the cascade emissions, which dominate the downconversion efficiency at low Tm^{3+} concentration, we use the branching ratios as determined by Yi *et al.*³⁸ for a crystal structure

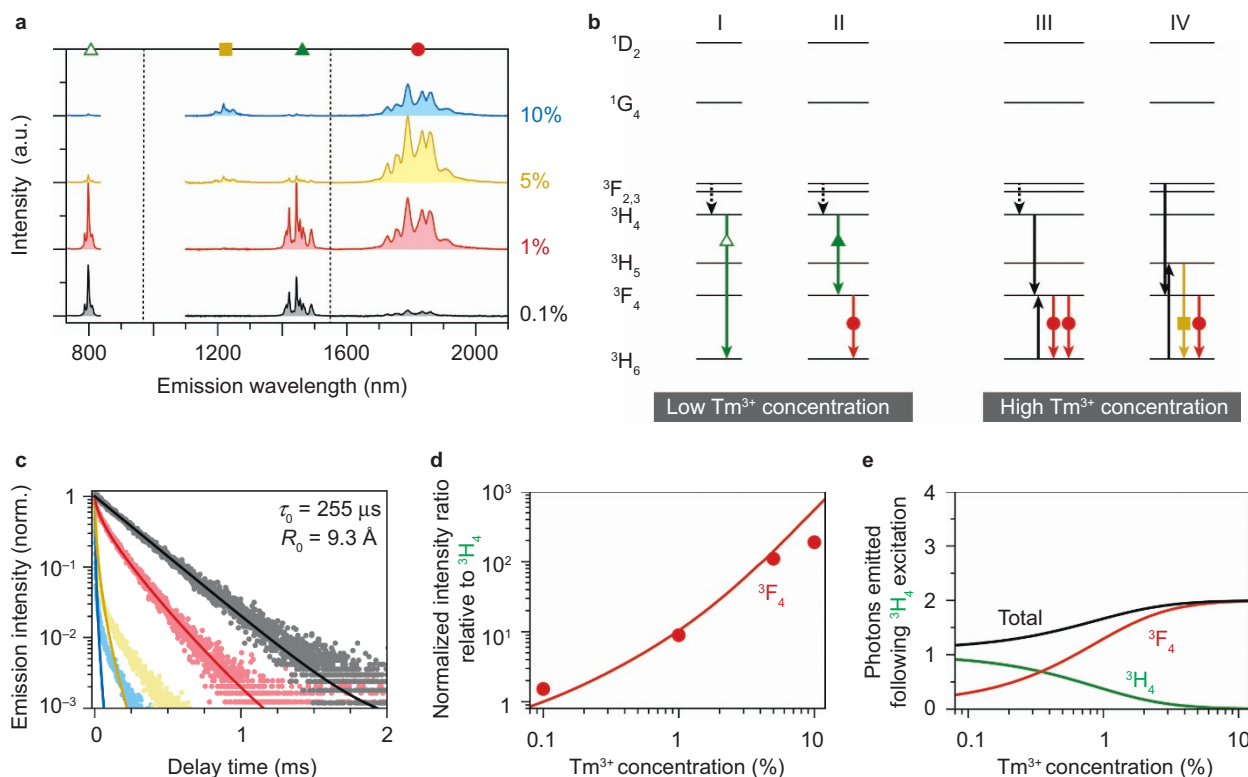


Figure 1 One-to-two downconversion from the $^3\text{F}_{2,3}$ and $^3\text{H}_4$ levels. **(a)** Emission spectra of $\text{Gd}_2\text{O}_2\text{S}:\text{Tm}^{3+}$ ($x\%$) with $x = 0.1$ (black), 1 (red), 5 (yellow), and 10 (blue) excited in the $^3\text{F}_{2,3}$ level at 697 nm. The spectra are recorded on three different detectors, as indicated by the vertical dashed lines, and are normalized for each detector individually. **(b)** Possible decay pathways of the Tm^{3+} $^3\text{F}_{2,3}$ excited state. Pathways I and II dominate at low Tm^{3+} concentrations; III and IV dominate at high concentrations. Multiphoton relaxation is depicted as dashed downward arrows, photon emission as colored arrows with symbols matching those marking emission lines in **a**, and cross-relaxation as black solid arrows. **(c)** Decay dynamics of the $^3\text{H}_4 \rightarrow ^3\text{H}_6$ emission at 800 nm upon excitation in the $^3\text{F}_{2,3}$ level at 697 nm. Solid lines are fit to Equation (2), from which we obtain an intrinsic lifetime of $\tau_0 = 255 \mu\text{s}$ and a critical radius for cross-relaxation of $R_0 = 9.3 \text{ \AA}$. **(d)** The ratio between the $^3\text{F}_4$ and $^3\text{H}_4$ emission intensities as obtained from the spectra shown in **a** (circles) normalized to the ratio at 0.1% Tm^{3+} . The solid line is the ratio expected based on the dynamics of **c**. **(e)** The theoretical absolute photon yields from the $^3\text{H}_4$ level (green), $^3\text{F}_4$ level (red), and the total yield (black) following excitation into the $^3\text{H}_4$ (or $^3\text{F}_{2,3}$) level.

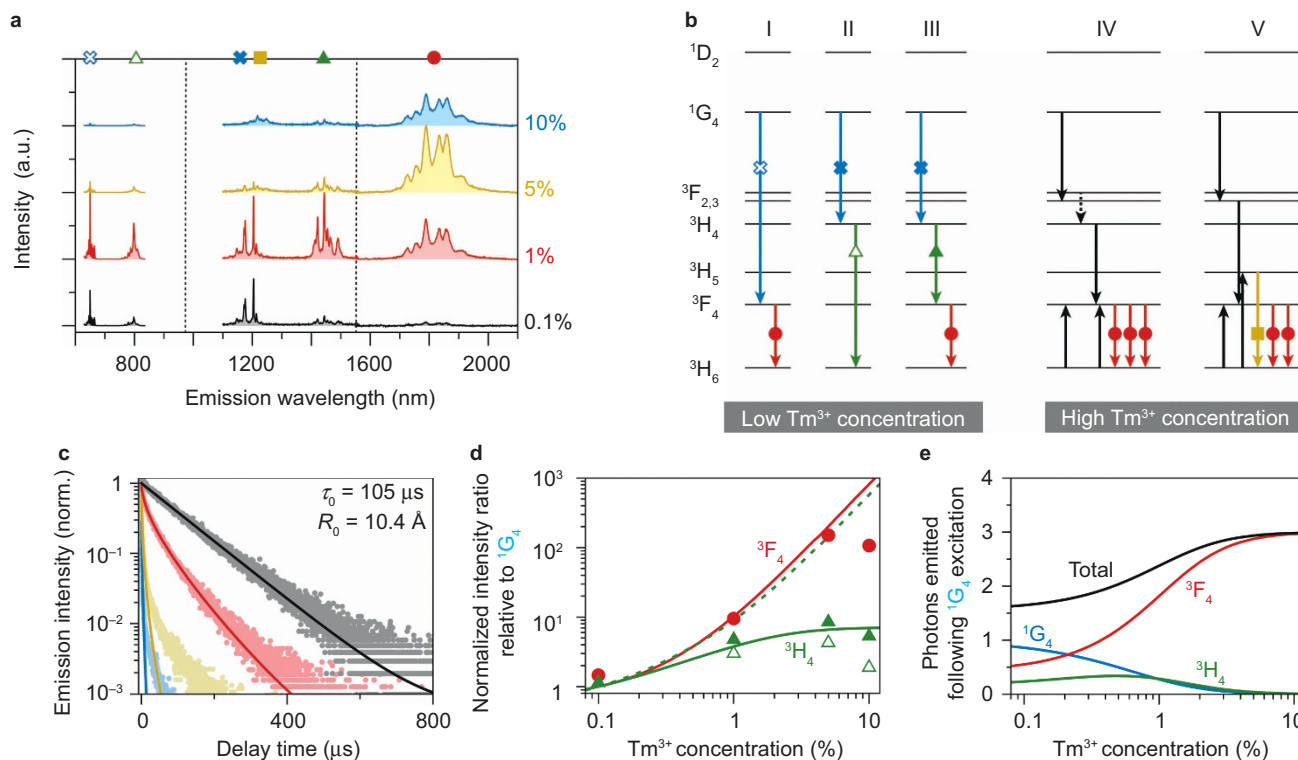


Figure 2 One-to-three downconversion from the 1G_4 level. **(a)** Emission spectra of Gd₂O₂S:Tm³⁺ ($x\%$) with $x = 0.1$ (black), 1 (red), 5 (yellow), and 10 (blue) excited in the 1G_4 level at 470 nm. They are recorded on three different detectors, as indicated by the vertical dashed lines, and are normalized for each detector individually. **(b)** Possible decay pathways of the Tm³⁺ 1G_4 excited state include cascade processes (pathways I, II, and III). At higher Tm³⁺ concentrations, ($^1G_4, ^3H_4$) \rightarrow ($^3F_{2,3}, ^3F_4$) cross-relaxation becomes the dominant decay pathway (IV and V), followed by further cross-relaxation from the $^3F_{3,2}$ and 3H_4 levels (see Figure 1). **(c)** The decay dynamics of the 1G_4 level in Gd₂O₂S:Tm³⁺ ($x\%$) with $x = 0.1$ (black), 1 (red), 5 (yellow), and 10 (blue), excited at 465 nm and detected for the $^1G_4 \rightarrow ^3F_4$ emission at 653 nm. Solid lines are fits to Equation (2), yielding an intrinsic lifetime of $\tau_0 = 105 \mu\text{s}$ and a critical radius for cross-relaxation of $R_0 = 10.4 \text{ \AA}$. **(d)** The intensity of emission from the 3F_4 (red circles) and 3H_4 (solid green triangle for $^3H_4 \rightarrow ^3F_4$, open green triangles for $^3H_4 \rightarrow ^3H_6$) levels relative to the 1G_4 level. Solid lines are the ratios as expected from our model (see Supplementary Information). The dashed green line would be the expected ratio of 3H_4 emission to 1G_4 emission if only the first step in the sequence of cross-relaxations occurred, i.e., ($^1G_4, ^3H_6$) \rightarrow ($^3F_{2,3}, ^3F_4$). The agreement with the experiment is very poor (compare to the green triangles), proving the occurrence of multiple cross-relaxation steps. **(e)** The total downconversion efficiency from the 1G_4 level (black line) and separated by emission from the 1G_4 (blue), 3H_4 (green), and 3F_4 (red) levels.

(Y₂O₃) similar to ours (Gd₂O₂S). For the cross-relaxation processes, which lead to efficient downconversion at high Tm³⁺ concentrations (>1%), we fit the excited state decay dynamics (see Figures 1c, 2c, and 3c) of the 3H_4 , 1G_4 , and 1D_2 levels to a model of first-order energy transfer^{17,22,39,40} (Equations (1) and (2)) and obtain values for the cross-relaxation strengths C_{xr} . From these, the cross-relaxation efficiency η_{xr} is calculated. For more details, see the Supplementary Information.

RESULTS AND DISCUSSION

One-to-two downconversion following excitation in the near-infrared

We start by examining the downconversion from the 3H_4 and $^3F_{2,3}$ levels of Tm³⁺. Figure 1a shows the emission spectra of Gd₂O₂S:Tm³⁺ ($x\%$) upon excitation in the $^3F_{2,3}$ level at 697 nm, from bottom to top for increasing Tm³⁺ concentration of $x = 0.1$ (black), 1 (red), 5 (yellow), and 10 (blue). The spectra are recorded on three separate detectors (boundaries indicated with vertical dashed lines) and are normalized for each detector separately. Consequently, the relative intensities of emission lines can be compared between different Tm³⁺ concentrations but not between different detectors. The emission lines are ascribed to the $^3H_4 \rightarrow ^3H_6$ transition at 800 nm, the $^3H_5 \rightarrow ^3H_6$ transition at 1215 nm, the $^3H_4 \rightarrow ^3F_4$ transition at 1450 nm, and the $^3F_4 \rightarrow ^3H_6$ transition at 1800 nm^{21,29,41}. At low

Tm³⁺ concentrations (0.1%, 1%), the emission is mainly from the 3H_4 level (lines indicated with a green triangle), whereas at higher concentrations (5%, 10%), emissions from 3H_5 (yellow square) and 3F_4 (red circle) dominate.

The observations are consistent with the relaxation pathways illustrated in Figure 1b. Pathways I and II dominate at low Tm³⁺ concentrations. Pathways III and IV, which involve cross-relaxation between pairs of ions and result in downconversion, become more likely at higher Tm³⁺ concentrations. Colored downward arrows represent photon emission, with symbols matching those marking the emission lines in Figure 1a. Fast non-radiative $^3F_{2,3} \rightarrow ^3H_4$ multi-phonon relaxation (dashed downward arrow) is evidenced by the absence of emission from the $^3F_{2,3}$ level. The occurrence of cross-relaxation processes (black solid arrows in pathways III and IV) is evidenced by the supralinear increase of emission intensity from the 3H_5 and 3F_4 levels with increasing Tm³⁺ concentration. Whereas radiative decay from the $^3F_{2,3}$ level cannot compete with multi-phonon relaxation, cross-relaxation at high Tm³⁺ concentrations (pathway IV) can, as evidenced by the observation of 3H_5 emission at 1215 nm. This indicates that very fast rates are possible for cross-relaxation processes in Gd₂O₂S:Tm³⁺. Indeed, Supplementary Fig. S2 shows that no 3H_5 emission is observed under excitation directly in the 3H_4 level (rather than in the $^3F_{2,3}$ level) because pathway IV is not

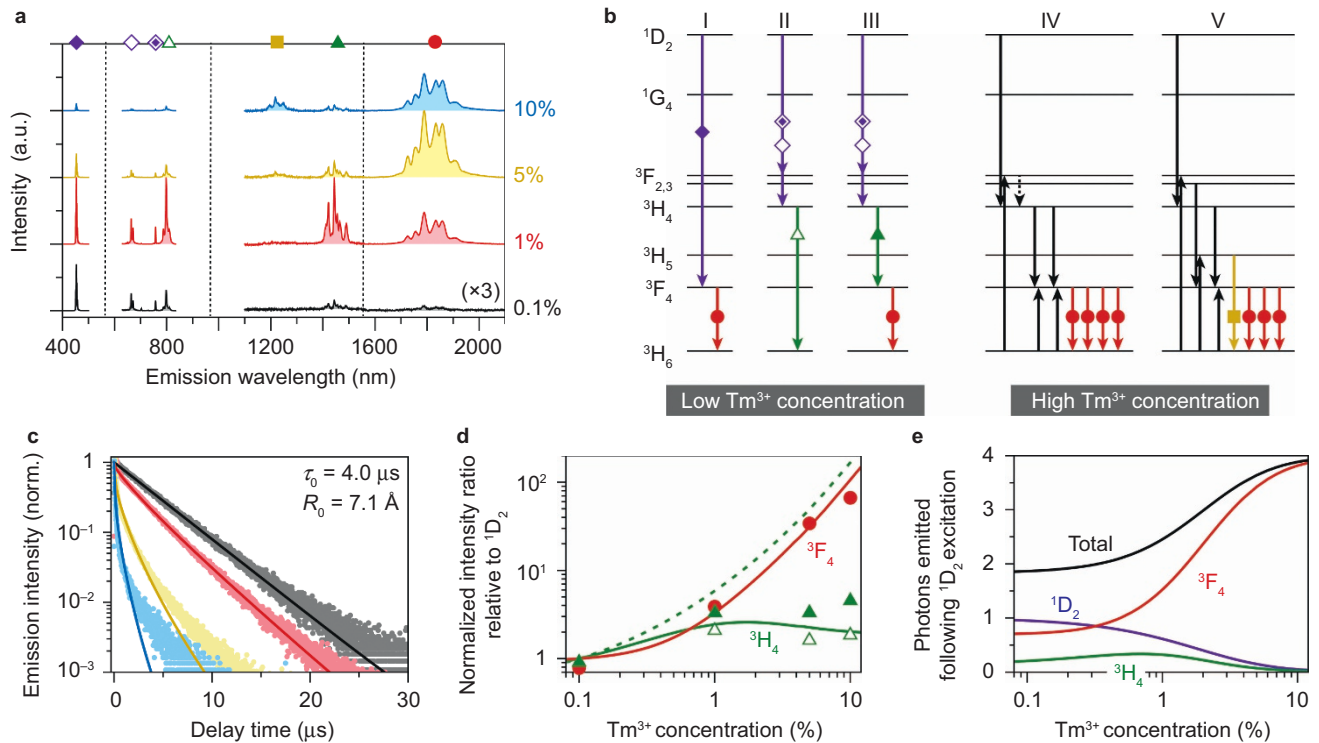


Figure 3 One-to-four downconversion from the $^1\text{D}_2$ level. **(a)** Emission spectra of $\text{Gd}_2\text{O}_2\text{S}:\text{Tm}^{3+}$ ($x\%$) with $x = 0.1$ (black), 1 (red), 5 (yellow), and 10 (blue) excited in the $^1\text{D}_2$ level at 365 nm. **(b)** Decay pathways from the $^1\text{D}_2$ level. Pathways I, II, and III involve cascade emission of photons (colored downward arrows marked with symbols corresponding to those in **a**) and are operative at low Tm^{3+} concentration. At high Tm^{3+} concentrations, cross-relaxation (solid black arrows in pathways IV and V) becomes more efficient, effectively cutting the excitation energy in four and leading to emission in the IR (yellow square and red circle in **a**). **(c)** PL decay curves of the $^1\text{D}_2$ level recorded at 465 nm ($^1\text{D}_2 \rightarrow ^3\text{F}_4$). Solid lines are fits to Equation (2), yielding an intrinsic lifetime of $\tau_0 = 4.0 \mu\text{s}$ for the $^1\text{D}_2$ level and a critical radius for cross-relaxation of $R_0 = 7.1 \text{ \AA}$. **(d)** The emission intensity from $^3\text{F}_4$ (red circles) and $^3\text{H}_4$ (green filled triangles: $^3\text{H}_4 \rightarrow ^3\text{F}_4$; green open triangles: $^3\text{H}_4 \rightarrow ^3\text{H}_6$) relative to $^1\text{D}_2$. Solid lines are the trends expected based on our model (see Supplementary Information). If we include only the first cross-relaxation step in our model (i.e., $(^1\text{D}_2, ^3\text{H}_6) \rightarrow (^3\text{H}_4, ^3\text{F}_{2,3})$), the predicted intensity ratio between $^3\text{H}_4$ and $^1\text{D}_2$ (dashed green line) deviates strongly from the experimental data points. **(e)** The total downconversion quantum yield (black line) following $^1\text{D}_2$ excitation. Emission comes mainly from the $^1\text{D}_2$ level at low Tm^{3+} concentrations and from $^3\text{F}_4$ at high Tm^{3+} concentrations. Consistent with the experiment **(a)**, emission from the $^3\text{H}_4$ level is brightest at intermediate concentrations of approximately 1%.

possible. This also proves that multi-phonon relaxation from $^3\text{H}_4$ to $^3\text{H}_5$ is negligible.

To quantify the rates and efficiencies of downconversion by cross-relaxation from the $^3\text{H}_4$ state, we recorded PL decay curves excited in the $^3\text{F}_{2,3}$ level (697 nm) and recorded at 800 nm at the $^3\text{H}_4 \rightarrow ^3\text{H}_6$ transition. Figure 1c shows that for increasing Tm^{3+} concentration, the decay of the $^3\text{H}_4$ level rapidly becomes faster, consistent with cross-relaxation (pathway III in Figure 1b). We fit the decay curve for 0.1% Tm^{3+} to a single exponential, assuming no cross-relaxation, and obtain an intrinsic lifetime of the $^3\text{H}_4$ level of $\tau_0 = 255 \mu\text{s}$. Next we assume that at higher Tm^{3+} concentrations, cross-relaxation can take place *via* dipole-dipole coupling in pairs of Tm^{3+} ions, yielding a cross-relaxation rate Γ_{xr} for a single pair proportional to the inverse sixth power of the separation r between the ions^{17,22,39,40}:

$$\Gamma_{\text{xr}} = C_{\text{xr}} r^{-6}. \quad (1)$$

The prefactor C_{xr} (which represents the strength of cross-relaxation) can alternatively be converted to a critical radius $R_0 = \sqrt[6]{\tau_0 C_{\text{xr}}}$, defined as the pair separation at which cross-relaxation has a 50% efficiency. We fit the decay curve for 1% Tm^{3+} to an analytical model that assumes a random substitution of Tm^{3+} for Gd^{3+} in the $\text{Gd}_2\text{O}_2\text{S}$ crystal^{139,40}:

$$I(t) = I(0)e^{-t/\tau_0} \prod_i^{\text{shells}} (1 - x + xe^{-C_{\text{xr}}t/r_i^6})^{n_i}, \quad (2)$$

where x is the Tm^{3+} acceptor concentration, and (r_i, n_i) represents the ‘neighbor list’ given by the crystal structure of $\text{Gd}_2\text{O}_2\text{S}$. The best fit is obtained for $C_{\text{xr}} = 2.5 \text{ nm}^6 \text{ ms}^{-1}$, corresponding to a critical radius of $R_0 = 9.3 \text{ \AA}$. This translates into a cross-relaxation rate in a nearest-neighbor pair (at a separation of 3.5 \AA ; one Tm^{3+} in the $^3\text{H}_4$ level and one in the $^3\text{H}_6$ ground state) of $1/0.75 \mu\text{s}$, 341 \times faster than radiative decay from the $^3\text{H}_4$ level. In Figure 1c, the solid lines through the data for 5% (yellow) and 10% (blue) Tm^{3+} are drawn following Equation (2) without additional fit parameters. They show a good match with the experimental PL decay curves. Deviations at high Tm^{3+} concentrations may be due to energy migration over the Tm^{3+} sublattice, reabsorption of emitted light, or upconversion processes (i.e., the inverse of cross-relaxation; see Supplementary Information for further discussion).

Based on the possible decay pathways of the $^3\text{H}_4$ level (Figure 1b) and with the assumption that no non-radiative loss occurs, we can estimate (see Supplementary Information for details) the expected light yield following excitation at 700–800 nm in the $^3\text{F}_{2,3}$ or $^3\text{H}_4$ level. Using the fitted value for the cross-relaxation strength C_{xr} (Figure 1c), we can estimate how the expected intensity ratio between $^3\text{F}_4$ and $^3\text{H}_4$ emission varies with Tm^{3+} concentration. In Figure 1d we plot the result (solid red line) and compare it to the experimental data (red circles). Efficient cross-relaxation causes the relative intensity in the IR at 1800 nm from the $^3\text{F}_4$ level to increase by more than a factor 100 as the Tm^{3+} concentration increases from 0.1% to 10%. Hence, our

model of ($^3\text{H}_4, ^3\text{H}_6$) \rightarrow ($^3\text{F}_4, ^3\text{F}_4$) cross-relaxation (Figure 1b) *via* dipole–dipole interaction is consistent with both the excited state dynamics (Figure 1c) and the resulting emission intensities (Figure 1d). The deviation between experiment and model that occurs in Figure 1d at 10% Tm^{3+} can be understood in terms of concentration quenching of the $^3\text{F}_4$ level (see the section on “Discussion”).

In Figure 1e, we plot the one-to-two downconversion quantum yield η_2 (see Supplementary Information) following excitation into the $^3\text{H}_4$ level as a function of Tm^{3+} concentration. We distinguish between photons emitted from the $^3\text{H}_4$ level and those emitted from the $^3\text{F}_4$ level based on our model and the fitted cross-relaxation strength C_{sr} . Whereas at low Tm^{3+} concentrations the emission comes primarily from the $^3\text{H}_4$ level (green line), at higher concentrations, $^3\text{F}_4$ emission (red line) is dominant. We see that $\text{Gd}_2\text{O}_2\text{S:Tm}^{3+}$ can efficiently downconvert photons of 800 nm. Because of cascade emission (pathway II in Figure 1b), η_2 is already over 100% (119%) at 0.1% Tm^{3+} ^{21,41,42}. It increases to 199% at 10% Tm^{3+} because cross-relaxation becomes much more efficient. Experimentally, the absolute downconversion quantum yield is difficult to determine quantitatively because emissions occur over such a large spectral range, including very close to the excitation wavelength and beyond the detector range. We can see in Figure 1a that the absolute emission intensity from the $^3\text{F}_4$ level decreases when the Tm^{3+} increases from 5% to 10%. This indicates that in our samples, concentration quenching effects (see the section on “Discussion”) are present at high Tm^{3+} concentrations, which diminish the actual quantum yields to below those estimated in Figure 1e.

One-to-three downconversion following blue excitation

Next, we investigate the efficiency of downconversion from the $^1\text{G}_4$ level of Tm^{3+} ⁴³. We perform a similar analysis as presented above in Figure 1 but for higher-energy excitation, to build a complete picture of the chain of cross-relaxation processes that can take place in $\text{Gd}_2\text{O}_2\text{S:Tm}^{3+}$. The $^1\text{G}_4$ level is excited with blue photons of 470 nm, which each provide enough energy to generate three IR photons of 1800 nm ($^3\text{F}_4 \rightarrow ^3\text{H}_6$). Figure 2a shows emission spectra of $\text{Gd}_2\text{O}_2\text{S:Tm}^{3+}$ following excitation in the $^1\text{G}_4$ level at 470 nm. In addition to the emission lines observed in Figure 1a from $^3\text{H}_4$ (green triangles), $^3\text{H}_5$ (yellow square), and $^3\text{F}_4$ (red circle), we now see emission from the $^1\text{G}_4$ level (blue crosses). The line at 650 nm is from the $^1\text{G}_4 \rightarrow ^3\text{F}_4$ transition, whereas the emission at approximately 1200 nm, observed at low Tm^{3+} concentrations (0.1%, 1%), originates from the $^1\text{G}_4 \rightarrow ^3\text{H}_4$ transition. At high Tm^{3+} concentrations (5%, 10%), the spectrum at approximately 1215 nm is of a different origin, namely the $^3\text{H}_5 \rightarrow ^3\text{H}_6$ transition, as evident from a comparison to Figure 1a. Overall, we see that at the lowest Tm^{3+} concentration (0.1%), the emission comes mainly from the $^1\text{G}_4$ level (blue crosses), at intermediate concentration (1%), $^3\text{H}_4$ emission is relatively strong (green triangles), whereas at high concentrations (5%, 10%) the spectrum is dominated by $^3\text{H}_5$ (yellow square) and $^3\text{F}_4$ (red circle) emissions.

Based on these observations, we propose relaxation pathways for the $^1\text{G}_4$ level as depicted in Figure 2b. At low Tm^{3+} concentrations, pathways I, II, and III result in cascade emissions from the $^1\text{G}_4$ level (there can also be direct radiative decay to the ground state, not depicted). At high Tm^{3+} concentrations, ($^1\text{G}_4, ^3\text{H}_6$) \rightarrow ($^3\text{F}_{2,3}, ^3\text{F}_4$) cross-relaxation occurs^{29,44}, after which the $^3\text{F}_{2,3}$ and $^3\text{H}_4$ excitations are further downconverted as already discussed in Figure 1. The result at high Tm^{3+} concentrations (5%, 10%) can be three IR emissions for each blue excitation, consistent with the dominant contribution from

the $^3\text{H}_5$ (yellow square) and $^3\text{F}_4$ (red circle) emissions in the spectra of Figure 2a. There may also be ($^1\text{G}_4, ^3\text{H}_6$) \rightarrow ($^3\text{H}_4, ^3\text{H}_5$) and ($^1\text{G}_4, ^3\text{H}_6$) \rightarrow ($^3\text{H}_5, ^3\text{H}_4$) cross-relaxation processes^{29,44}, which would lead to similar downconversion schemes, except that the $^3\text{H}_5$ level is directly populated in the first step of the sequence of cross-relaxation steps. Because we experimentally observe $^3\text{H}_5$ emission only at the highest concentrations, the dominant first cross-relaxation process is probably ($^1\text{G}_4, ^3\text{H}_6$) \rightarrow ($^3\text{F}_{2,3}, ^3\text{F}_4$).

We investigate the downconversion dynamics of the $^1\text{G}_4$ level, as shown in Figure 2c. The solid lines are fits of the experimental data (symbols) to the model of cross-relaxation by dipole–dipole coupling (Equation (2)). We obtain for the $^1\text{G}_4$ level an intrinsic lifetime of $\tau_0 = 105 \mu\text{s}$ and a cross-relaxation strength of $C_{\text{sr}} = 11.8 \text{ nm}^6 \text{ ms}^{-1}$, corresponding to a critical radius of $R_0 = 10.4 \text{ \AA}$. This means that the cross-relaxation rate of the $^1\text{G}_4$ level in a nearest-neighbor pair is $1/0.16 \mu\text{s}$, $660\times$ faster than radiative decay. Such fast cross-relaxation rates explain why in upconversion experiments only low Tm^{3+} concentrations of no higher than 1% yield bright blue upconversion emission^{44–46}.

As we did in Figure 1d for $^3\text{H}_4$ excitation, with the fit results on the decay dynamics (Figure 2c), we can calculate the theoretical photon yields upon $^1\text{G}_4$ excitation (see Supplementary Information). Figure 2d shows the intensity ratio of $^3\text{F}_4$ (red) or $^3\text{H}_4$ (green) emission to $^1\text{G}_4$ emission. The experimental data (data points) show a good match to the theoretical predictions (solid lines). This confirms the occurrence of the sequence of cross-relaxation processes depicted in Figure 2b, which lead to the generation of three IR photons for each blue excitation. As a check, the dashed green line in Figure 2d shows the expected $^3\text{H}_4$ -to- $^1\text{G}_4$ intensity ratio in the hypothetical case that only the first cross-relaxation process occurred (i.e., ($^1\text{G}_4, ^3\text{H}_6$) \rightarrow ($^3\text{F}_{2,3}, ^3\text{F}_4$)) rather than a sequence of two cross-relaxation steps. This scenario is not consistent with the experimental emission spectra.

In Figure 2e, we plot the absolute photon yields following $^1\text{G}_4$ excitation, as calculated with our model (see Supplementary Information). At low Tm^{3+} concentrations, the emission comes mainly from the $^1\text{G}_4$ level (blue line), although through cascade processes (pathways I, II, III in Figure 2b), the other levels emit as well. Consistent with the experimental spectra (Figure 2a), emission comes primarily from the $^3\text{F}_4$ level (red line) at high Tm^{3+} concentrations. The total downconversion efficiency increases from 165% at 0.1% Tm^{3+} (by virtue of cascade emissions) to 298% at 10% (determined by cross-relaxation). In practice the absolute photon yield is limited by concentration quenching of the $^3\text{F}_4$ emission at high Tm^{3+} concentrations.

One-to-four downconversion following UV excitation

Finally, we increase the excitation energy further to be resonant with the $^1\text{D}_2$ level of Tm^{3+} . Excitation photons in the UV (of 365 nm) have sufficient energy to yield as many as four IR photons from the $^3\text{F}_4$ level. Figure 3a shows the emission spectra of $\text{Gd}_2\text{O}_2\text{S:Tm}^{3+}$ excited in the $^1\text{D}_2$ level at 365 nm. We observe emission from the $^1\text{D}_2$ level (purple diamonds) and, at higher Tm^{3+} concentrations, from $^3\text{H}_4$ (green triangles), $^3\text{H}_5$ (yellow square), and $^3\text{F}_4$ (red circle) but not from the $^1\text{G}_4$ level (compare Figure 2a). This indicates that cross-relaxation processes occur but not to the $^1\text{G}_4$ level. Moreover, we can conclude that multi-phonon relaxation from $^1\text{D}_2$ to $^1\text{G}_4$ is negligible.

In Figure 3b, we depict the decay pathways from the $^1\text{D}_2$ level dominant in $\text{Gd}_2\text{O}_2\text{S:Tm}^{3+}$. At low Tm^{3+} concentrations there are possibilities for cascade emission (pathways I, II, and III)^{29,46–48}. At high Tm^{3+} concentrations, because we see in the emission spectrum

that cross-relaxation to the $^1\text{G}_4$ level is not efficient, the dominant process must be $(^1\text{D}_2, ^3\text{H}_6) \rightarrow (^3\text{H}_4, ^3\text{F}_{2,3})$, as depicted in pathways IV and V^{29,44}. After reaching the $^3\text{H}_4$ and $^3\text{F}_{2,3}$ levels, the Tm^{3+} ions decay further, by cross-relaxation, as discussed above in Figure 1. The result can be as many as four emitted IR photons (red circles and yellow squares) for each UV excitation.

Figure 3c shows the decay dynamics of the $^1\text{D}_2$ level recorded for the $^1\text{D}_2 \rightarrow ^3\text{F}_4$ emission at 465 nm. We again apply our model of cross-relaxation by dipole–dipole interaction (Equation (2)) to fit the dynamics. The best fit is obtained for an intrinsic lifetime of $\tau_0 = 4.0 \mu\text{s}$ and a cross-relaxation strength of $C_{\text{xr}} = 32.8 \text{ nm}^6 \text{ ms}^{-1}$ (corresponding to a critical radius of $R_0 = 7.1 \text{ \AA}$, and a nearest-neighbor cross-relaxation rate of $1/0.06 \mu\text{s}$, $69\times$ faster than the intrinsic decay). Hence, this cross-relaxation process from the $^1\text{D}_2$ level is less efficient than those from the $^3\text{H}_4$ (Figure 1c) and $^1\text{G}_4$ levels (Figure 2c) but still competes strongly with radiative decay.

To confirm the occurrence of one-to-four downconversion in $\text{Gd}_2\text{O}_2\text{S}:\text{Tm}^{3+}$ via the scheme of three cross-relaxation steps (Figure 3b), we compare the relative emission intensities in the spectra to the predictions of our model (see Supplementary Information). Figure 3d shows a good correspondence between the experiment (data points) and the model (solid lines). Downconversion occurs at low Tm^{3+} concentrations because of several possible cascade processes (pathways I, II and III in Figure 3b). Nevertheless, the relative intensity of $^3\text{F}_4$ emission increases by a factor 100 as the Tm^{3+} increases from 0.1% to 10%. As a check, we can see that if we do not include the second and third steps of the sequence of cross-relaxations, the agreement between model and experiment is very poor (dashed green line).

Figure 3e presents the theoretical photon yield for excitation in the $^1\text{D}_2$ level. At the low Tm^{3+} concentration of 0.1%, the downconversion quantum yield is as high as 186% by virtue of the many possible cascade processes (pathways I, II, and III in Figure 3b), through which the UV excitation can relax⁴². The downconversion quantum yield increases to 388% at 10% Tm^{3+} because the cross-relaxation becomes more efficient. By comparing the absolute emission intensities (Figure 3a) from the $^3\text{F}_4$ level for 5% and 10% Tm^{3+} , it becomes apparent that concentration quenching effects are at play at the highest

Tm^{3+} concentrations, which reduce the effective downconversion yield (see the section on “Discussion”).

Discussion

Our results highlight $\text{Gd}_2\text{O}_2\text{S}:\text{Tm}^{3+}$ as a promising material to efficiently downconvert the near-IR, visible, and UV part of the spectrum to IR photons. Two challenges have to be solved for this material to significantly enhance the photo-response of next-generation solar cells: (i) the relatively weak absorption of Tm^{3+} and (ii) concentration quenching of the $^3\text{F}_4$ level.

The absorption spectrum of Tm^{3+} , as for most other trivalent lanthanide ions, contains a few narrow lines originating from the intra-configurational transitions from the $^3\text{H}_6$ ground state to the many possible excited states. In the inset of Figure 4a, we show the excitation spectra of Tm^{3+} for the $^3\text{H}_4 \rightarrow ^3\text{F}_4$ emission. The absorptions are relatively weak and narrow. A more detailed investigation of the different line intensities in the full excitation spectrum, as a function of Tm^{3+} concentration, is presented in Supplementary Fig. S3. To increase the effective absorption strength of Tm^{3+} and make it broadband, sensitizers are needed^{20,47–50}. For example, the material could be co-doped with strongly absorbing centers, such as Ce^{3+} , for sensitization^{20,39,49,50}. Such schemes allow for the absorption spectrum of the material to be tuned independently of the downconversion process. This opens up interesting but challenging possibilities, such as materials that convert UV and near-IR to IR photons but are transparent to visible light for use as luminescent solar concentrators in windows.

Figure 4a shows the fraction of the solar spectrum made available through downconversion, if we assume broadband effective absorption of Tm^{3+} by means of sensitization. We consider a solar cell with a bandgap of 0.65 eV (1900 nm; e.g., Ge)¹¹ such that all $^3\text{F}_4$ emission can be absorbed. The red area in Figure 4a is directly usable by this solar cell. In the ideal sensitized downconverter (based on the excitation spectrum of Tm^{3+} ; Supplementary Fig. S3 and the inset of Figure 4a), all photons with energy higher than $h\nu > 3.36 \text{ eV}$ are funneled to the $^1\text{D}_2$ level, photons of $2.59 \text{ eV} < h\nu < 3.36 \text{ eV}$ to the $^1\text{G}_4$ level, and photons of $1.50 \text{ eV} < h\nu < 2.59 \text{ eV}$ to the $^3\text{H}_4$ level. The colored areas in Figure 4a indicate the gain enabled by one-to-two (green),

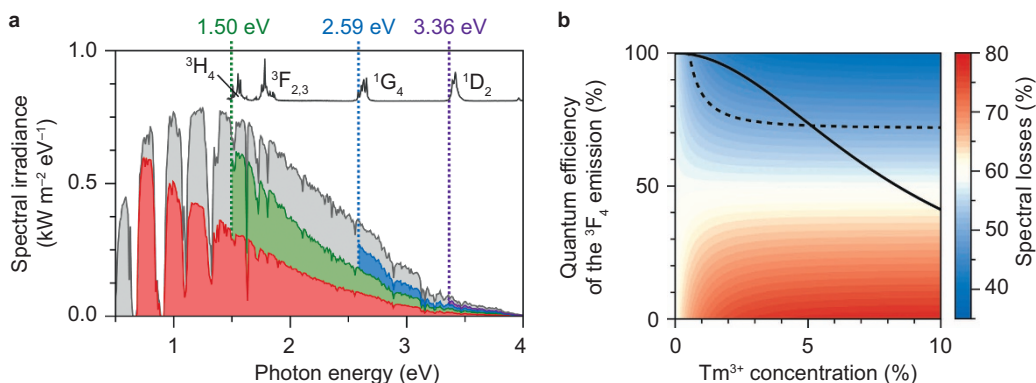


Figure 4 Reducing spectral mismatch losses with $\text{Gd}_2\text{O}_2\text{S}:\text{Tm}^{3+}$. (a) A simple solar cell with a band gap of 0.65 eV (1900 nm; for example, Ge) can effectively use only the part of the solar spectrum shaded red. Spectral conversion by a sensitized downconverter layer of $\text{Gd}_2\text{O}_2\text{S}:\text{Tm}^{3+}$ would make additional parts available: the green part by one-to-two downconversion from the $^3\text{H}_4$ level, the blue part by one-to-three downconversion from the $^1\text{G}_4$ level, and the purple part by one-to-four downconversion from the $^1\text{D}_2$ level. The inset shows the positions of the various absorption lines in $\text{Gd}_2\text{O}_2\text{S}:\text{Tm}^{3+}$ in the excitation spectrum of the $^3\text{H}_4 \rightarrow ^3\text{F}_4$ emission at 1450 nm. (b) The calculated spectral losses as a function of the Tm^{3+} concentration in $\text{Gd}_2\text{O}_2\text{S}$ and the quantum efficiency η_{em} of the IR emission from the $^3\text{F}_4$ level. The solid black line shows how η_{em} varies with the Tm^{3+} concentration according to Equation (3), and assuming a critical concentration of $x_0 = 10\%$. For the actual crystal, where the concentration quenching is directly linked to the Tm^{3+} concentration, as described by Equation (3), the spectral losses as a function of the Tm^{3+} concentration are the color values at the position of the solid line. They are lowest (42%) at 2–3% Tm^{3+} . The dashed line is the contour corresponding to the spectral losses of 50% for a crystalline Si solar cell (band gap = 1.1 eV). We see that a $\text{Gd}_2\text{O}_2\text{S}:\text{Tm}^{3+}$ with a Ge solar cell can outperform crystalline Si.

one-to-three (blue), and one-to-four (purple) downconversion. The spectral mismatch losses are reduced from 59% in the bare solar cell to 37% in combination with the downconverter (compared to 50% for a Si solar cell).

The essential last step of the downconversion is the emission of photons from the ³F₄ level. As apparent from the relatively low absolute emission intensities at 10% Tm³⁺ (Figures 1a, 2a, and 3a), the ³F₄ level is partially quenched at this concentration. This can be ascribed to concentration quenching, i.e., migration of the excitation energy over the Tm³⁺ sublattice until it reaches a quenching site. The effect has been studied in detail by Auzel *et al.*⁵¹ for the lowest excited state of Yb³⁺, Er³⁺, and Ho³⁺ in the crystalline host material Y₂O₃. They used a model where the PL quantum efficiency of emission depends on the concentration of luminescent ions x as

$$\eta_{\text{em}}(x) = \left[1 + \frac{9}{2\pi} \left(\frac{x}{x_0} \right)^2 \right]^{-1}, \quad (3)$$

where x_0 is the critical concentration. Auzel *et al.* found critical concentrations of approximately $x_0 \approx 10\%$ for the three ions investigated⁵¹. The effect of concentration quenching in a crystal doped with luminescent ions depends on the material quality⁵². With our equipment, we are unable to measure η_{em} for the IR emission from the lowest excited state of Tm³⁺ in our samples, but the values could be expected to follow the same trend as those found by Auzel *et al.* for Yb³⁺, Er³⁺, and Ho³⁺ in Y₂O₃⁵⁰.

In Figure 4b, we plot how spectral losses of the situation depicted Figure 4a (solar cell of band gap 0.65 eV plus Gd₂O₂S:Tm³⁺ downconverter) would depend on the Tm³⁺ concentration and η_{em} of the ³F₄ level. The lowest spectral losses require a high Tm³⁺ concentration (for efficient cross-relaxation) and a high η_{em} . Because, as described by Equation (3), high Tm³⁺ concentrations come with a lower η_{em} , there is some optimum concentration. The solid black line in Figure 4b depicts how η_{em} would vary with Tm³⁺ concentration according to Equation (3) with $x_0 = 10\%$. The lowest spectral losses are 42% at a Tm³⁺ concentration of 2–3%, significantly lower than the 59% for the bare solar cell with a band gap of 0.65 eV and even lower than Si (50%; dashed line).

CONCLUSION

To summarize, we have demonstrated that Tm³⁺ in Gd₂O₂S can effectively downconvert high-energy photons from the near-IR, visible and UV to IR photons of a wavelength of 1800 nm. By virtue of a variety of cross-relaxation processes, an excitation in the ³H₄ level (800 nm) can be converted to two IR photons, from the ¹G₄ level (470 nm) to three and from the ¹D₂ level (365 nm) to four. We have quantified the cross-relaxation rates and efficiencies for different Tm³⁺ concentrations by fitting the decay dynamics of the levels involved. For the three downconversion processes, the efficiencies are near 200%, 300%, and 400% for 10% Tm³⁺. These results are consistent with the relative intensities of the emission lines as found experimentally. We have discussed the potential application of Gd₂O₂S:Tm³⁺ as a spectral converter for photovoltaics. In particular, this material could greatly improve the efficiency of Ge solar cells, to such extent that they could even outperform crystalline Si in terms of spectral mismatch losses.

ACKNOWLEDGEMENTS

Financial support from the National Science Foundation of China (51125005 and 51472088) is gratefully acknowledged. Dechao Yu thanks the China Scholarship Council (CSC, File No. 201206150022) for a scholarship. This

work is part of the research program of the ‘Stichting voor Fundamenteel Onderzoek der Materie (FOM)’, which is financially supported by the ‘Nederlandse Organisatie voor Wetenschappelijk Onderzoek (NWO)’.

- 1 Wegh RT, Donker H, Oskam KD, Meijerink A. Visible quantum cutting in LiGdF₄:Eu³⁺ through downconversion. *Science* 1999; **283**: 663–666.
- 2 Zhang QY, Huang XY. Recent progress in quantum cutting phosphors. *Prog Mater Sci* 2010; **55**: 353–427.
- 3 Dexter DL. Possibility of luminescent quantum yield greater than unity. *Phys Rev* 1957; **108**: 630–633.
- 4 Jüstel T, Nikol H. Optimization of luminescent materials for plasma display panels. *Adv Mater* 2000; **12**: 527–530.
- 5 Feldmann C, Jüstel T, Ronda CR, Schmidt PJ. Inorganic luminescent materials: 100 years of research and application. *Adv Funct Mater* 2003; **13**: 511–516.
- 6 Lee TJ, Luo LY, Diao EWG, Chen TM, Cheng BM *et al.* Visible quantum cutting through downconversion in green-emitting K₂GdF₅:Tb³⁺ phosphors. *Appl Phys Lett* 2006; **89**: 131121.
- 7 Trupke T, Green MA, Würfel P. Improving solar cell efficiencies by down-conversion of high-energy photons. *J Appl Phys* 2002; **92**: 1668–1674.
- 8 Richards BS. Luminescent layers for enhanced silicon solar cell performance: down-conversion. *Sol Energy Mater Sol Cells* 2006; **90**: 1189–1270.
- 9 van der Ende BM, Aarts L, Meijerink A. Lanthanide ions as spectral converters for solar cells. *Phys Chem Chem Phys* 2009; **11**: 11081–11095.
- 10 Abrams ZR, Niv A, Zhang X. Solar energy enhancement using down-converting particles: a rigorous approach. *J Appl Phys* 2011; **109**: 114905.
- 11 ten Kate OM, de Jong M, Hintzen HT, van der Kolk E. Efficiency enhancement calculations of state-of-the-art solar cells by luminescent layers with spectral shifting, quantum cutting, and quantum tripling function. *J Appl Phys* 2013; **114**: 084502.
- 12 Luque A. Will we exceed 50% efficiency in photovoltaics? *J Appl Phys* 2011; **110**: 031301.
- 13 Shockley W, Queisser HJ. Detailed balance limit of efficiency of p-n junction solar cells. *J Appl Phys* 1961; **32**: 510–519.
- 14 Polman A, Atwater HA. Photonic design principles for ultrahigh-efficiency photovoltaics. *Nat Mater* 2012; **11**: 174–177.
- 15 Marti A, Araújo GL. Limiting efficiencies for photovoltaic energy conversion in multigap systems. *Sol Energy Mater Sol Cells* 1996; **43**: 203–222.
- 16 Green MA, Emery K, Hishikawa Y, Warta W. Solar cell efficiency tables (version 33). *Prog Photovolt: Res Appl* 2009; **17**: 85–94.
- 17 Vergeer P, Vlught TJH, Kox MHF, den Hertog MI, van der Eerden JPJM *et al.* Quantum cutting by cooperative energy transfer in Yb_xY_{1-x}PO₄:Tb³⁺. *Phys Rev B* 2005; **71**: 014119.
- 18 Zhang QY, Yang GF, Jiang ZH. Cooperative downconversion in GdAl₃(BO₃)₄:RE³⁺, Yb³⁺ (RE = Pr, Tb, and Tm). *Appl Phys Lett* 2007; **91**: 051903.
- 19 Ye S, Zhu B, Luo J, Chen JX, Lakshminarayana G *et al.* Enhanced cooperative quantum cutting in Tm³⁺-Yb³⁺ codoped glass ceramic containing LaF₃ nanocrystals. *Opt Express* 2008; **16**: 8989–8994.
- 20 van der Ende BM, Aarts L, Meijerink A. Near-infrared quantum cutting for photovoltaics. *Adv Mater* 2009; **21**: 3073–3077.
- 21 Yu DC, Zhang JP, Chen QJ, Zhang WJ, Yang ZM *et al.* Three-photon near-infrared quantum cutting in Tm³⁺-doped transparent oxyfluoride glass ceramics. *Appl Phys Lett* 2012; **101**: 171108.
- 22 van Wijngaarden JT, Scheidelaar S, Vlught TJH, Reid MF, Meijerink A. Energy transfer mechanism for downconversion in the (Pr³⁺, Yb³⁺) couple. *Phys Rev B* 2010; **81**: 155112.
- 23 Zheng W, Zhu HM, Li RF, Tu DT, Liu YS *et al.* Visible-to-infrared quantum cutting by phonon-assisted energy transfer in YPO₄:Tm³⁺, Yb³⁺ phosphors. *Phys Chem Chem Phys* 2012; **14**: 6974–6980.
- 24 Eilers JJ, Biner D, van Wijngaarden JT, Krämer K, Güdel HU *et al.* Efficient visible to infrared quantum cutting through downconversion with the Er³⁺-Yb³⁺ couple in Cs₃Y₂Br₉. *Appl Phys Lett* 2010; **96**: 151106.
- 25 Miritello M, Savio RL, Cardile P, Priolo F. Enhanced down conversion of photons emitted by photoexcited Er_xY_{2-x}Si₂O₇ films grown on silicon. *Phys Rev B* 2010; **81**: 041411(R).
- 26 Yu DC, Huang XY, Ye S, Peng MY, Zhang QY *et al.* Three-photon near-infrared quantum splitting in β-NaYF₄:Ho³⁺. *Appl Phys Lett* 2011; **99**: 161904.
- 27 Chen DQ, Wang YS, Hong MC. Lanthanide nanomaterials with photon management characteristics for photovoltaic application. *Nano Energy* 2012; **1**: 73–90.
- 28 Yu DC, Ye S, Huang XY, Zhang QY. Enhanced three-photon near-infrared quantum splitting in β-NaYF₄:Ho³⁺ by codoping Yb³⁺. *AIP Adv* 2012; **2**: 022124.
- 29 Chen XB, Salamo GJ, Yang GJ, Li YL, Ding XL *et al.* Multiphoton near-infrared quantum cutting luminescence phenomena of Tm³⁺ ion in (Y_{1-x}Tm_x)₃Al₅O₁₂ powder phosphor. *Opt Express* 2013; **21**: A829–A840.
- 30 Timmerman D, Valenta J, Dohnalová K, de Boer WDAM, Gregorkiewicz T. Step-like enhancement of luminescence quantum yield of silicon nanocrystals. *Nat Nanotechnol* 2011; **6**: 710–713.
- 31 Tabachnyk M, Ehrler B, Gélineas S, Böhm ML, Walker BJ *et al.* Resonant energy transfer of triplet excitons from pentacene to PbSe nanocrystals. *Nat Mater* 2014; **13**: 1033–1038.

- 32 Thompson NJ, Wilson MWB, Congreve DN, Brown PR, Scherer JM *et al*. Energy harvesting of non-emissive triplet excitons in tetracene by emissive PbS nanocrystals. *Nat Mater* 2014; **13**: 1039–1043.
- 33 Abrams ZR, Charghi M, Niv A, Gladden C, Zhang X. Theoretical efficiency of 3rd generation solar cells: comparison between carrier multiplication and down-conversion. *Sol Energy Mater Sol Cells* 2012; **99**: 308–315.
- 34 Naczynski DJ, Tan MC, Zevon M, Wall B, Kohl J *et al*. Rare-earth-doped biological composites as *in vivo* shortwave infrared reporters. *Nat Commun* 2013; **4**: 2199.
- 35 Bashkatov AN, Genina EA, Kochubey VI, Tuchin VV. Optical properties of human skin, subcutaneous and mucous tissues in the wavelength range from 400 to 2000 nm. *J Phys D: Appl Phys* 2005; **38**: 2543–2555.
- 36 Eick HA. The preparation, lattice parameters and some chemical properties of the rare earth mono-thio oxides. *J Am Chem Soc* 1958; **80**: 43–44.
- 37 Martín-Rodríguez R, Fischer S, Ivaturi A, Froehlich B, Krämer KW *et al*. Highly efficient IR to NIR upconversion in $\text{Gd}_2\text{O}_2\text{S:Er}^{3+}$ for photovoltaic applications. *Chem Mater* 2013; **25**: 1912–1921.
- 38 Yi Q, Tsuboi T, Zhou S, Nakai Y, Lin H *et al*. Investigation of emission properties of $\text{Tm}^{3+}:\text{Y}_2\text{O}_3$ transparent ceramic. *Chin Opt Lett* 2012; **10**: 091602.
- 39 Rabouw FT, den Hartog SA, Senden T, Meijerink A. Photonic effects on the Förster resonance energy transfer efficiency. *Nat Commun* 2014; **5**: 3610.
- 40 Yu DC, Rabouw FT, Boon WQ, Kieboom T, Ye S *et al*. Insights into the energy transfer mechanism in $\text{Ce}^{3+}\text{-Yb}^{3+}$ codoped YAG phosphors. *Phys Rev B* 2014; **90**: 165126.
- 41 Yu DC, Ye S, Peng MY, Zhang QY, Wondraczek L. Sequential three-step three-photon near-infrared quantum splitting in $\beta\text{-NaYF}_4\text{:Tm}^{3+}$. *Appl Phys Lett* 2012; **100**: 191911.
- 42 O'Connor R, Mahiou R, Martinant D, Fournier MT. Luminescence and dynamics in $\text{Tm}^{3+}:\text{NaYF}_4$. *J Alloys Compd* 1995; **225**: 107–110.
- 43 ten Kate OM, van der Kolk E. Quantum tripling in Tm^{3+} -doped $\text{La}_2\text{BaZnO}_5$ phosphors for efficiency enhancement of small bandgap solar cells. *J Lumin* 2014; **156**: 262–265.
- 44 Thrash RJ, Johnson LF. Upconversion laser emission from Yb^{3+} -sensitized Tm^{3+} in BaY_2F_8 . *J Opt Soc Am B* 1994; **11**: 881–885.
- 45 Zhao JB, Jin DY, Schartner EP, Lu YQ, Liu YJ *et al*. Single-nanocrystal sensitivity achieved by enhanced upconversion luminescence. *Nat Nanotechnol* 2013; **8**: 729–734.
- 46 Wang F, Deng RR, Wang J, Wang QX, Han Y *et al*. Tuning upconversion through energy migration in core-shell nanoparticles. *Nat Mater* 2011; **10**: 968–973.
- 47 Wang YZ, Yu DC, Lin HH, Ye S, Peng MY *et al*. Broadband three-photon near-infrared quantum cutting in Tm^{3+} singly doped YVO_4 . *J Appl Phys* 2013; **114**: 203510.
- 48 Chen XB, Li S, Salamo GJ, Li YL, He LZ *et al*. Sensitized intense near-infrared downconversion quantum cutting three-photon luminescence phenomena of the Tm^{3+} ion activator in $\text{Tm}^{3+}\text{Bi}^{3+}:\text{YNbO}_4$ powder phosphor. *Opt Express* 2015; **23**: A51–A61.
- 49 Dong SL, Lin HH, Yu T, Zhang QY. Near-infrared quantum-cutting luminescence and energy transfer properties of $\text{Ca}_3(\text{PO}_4)_2\text{:Tm}^{3+},\text{Ce}^{3+}$ phosphors. *J Appl Phys* 2014; **116**: 023517.
- 50 Zhang GG, Liu CM, Wang J, Kuang XJ, Su Q. A dual-mode solar spectral converter $\text{CaLaGa}_3\text{S}_6\text{:Ce}^{3+},\text{Pr}^{3+}$: UV-Vis-NIR luminescence properties and solar spectral converting mechanism. *J Mater Chem* 2012; **22**: 2226–2232.
- 51 Auzel F, Baldacchini G, Laversenne L, Boulon G. Radiation trapping and self-quenching analysis in Yb^{3+} , Er^{3+} , and Ho^{3+} doped Y_2O_3 . *Opt Mater* 2003; **24**: 103–109.
- 52 Martín-Rodríguez R, Rabouw FT, Trevisani M, Bettinelli M, Meijerink A. Upconversion dynamics in Er^{3+} -doped $\text{Gd}_2\text{O}_2\text{S}$: influence of excitation power, Er^{3+} concentration, and defects. *Adv Optical Mater* 2015; **3**: 558–567.



This work is licensed under a Creative Commons Attribution-NonCommercial-NoDerivs 4.0 Unported License. The images or other third party material in this article are included in the article's Creative Commons license, unless indicated otherwise in the credit line; if the material is not included under the Creative Commons license, users will need to obtain permission from the license holder to reproduce the material. To view a copy of this license, visit <http://creativecommons.org/licenses/by-nc-nd/4.0/>

Supplementary information for this article can be found on the *Light: Science & Applications*' website (<http://www.nature.com/lsa>).